RSC Advances



PAPER

View Article Online
View Journal | View Issue



Cite this: RSC Adv., 2025, 15, 28805

Dynamic covalent interaction induced formation of a bortezomib—andrographolide complex and construction of the dual-drug delivery system

Shihui Qiao,†^a Hui Long,†^{abc} Yun Song,†*^a Xu Dong,†*^{ab} Huamin Zhong,^a Huanfeng Meng,^a Jingwen Gong,^a Yong Wang,^a Yiheng Liu,^d Haiying Zhang*^{abc} and Lujia Mao ¹ **

The interaction of boronic acids and 1,3-diols has significant application in tumour targeting and transcellular transfer, potentially to be employed in developing drug delivery systems. Bortezomib (BTZ), the dipeptide boronic acid analogue, is an FDA-approved anti-tumour drug. The hydrophobic boronic acid skeleton on BTZ resulted in unfavorable pharmacokinetic properties, which limits its efficacy for the treatment of solid tumours. Andrographolide (AND) holds significant potential for clinical application as a cancer treatment. The ¹H and ¹¹B NMR proved that BTZ-AND was formed via the interaction of a 1,3diol moiety on AND with the boronic acid skeleton on BTZ. The CCK-8 tests suggested that BTZ-AND exhibited broad-spectrum anti-tumour effects on two types of solid tumours (U251 glioma cells and A549 cells). Additionally, BTZ-AND had a moderate binding affinity towards bovine serum albumin (BSA, the binding constant K_a as 1.16×10^4 L mol⁻¹ at 25 °C). Hydrophobic interactions are dominant in stabilizing the (BTZ-AND)-BSA complex due to the positive ΔH and ΔS , which was further proved by molecular docking results. These findings inspired us to develop the protocol for the delivery of BTZ-AND with BSA nanoparticles, which is capable of improving the pharmacokinetic properties, such as solubility and stability. When U251 glioma cells and A549 cells were treated with Ce6 labeled BTZ-AND@BSA NPs, it demonstrated notable potential in cellular uptake. Herein, we established a robust theoretical and experimental foundation for the advancement of dual drug delivery systems, presenting a promising basis for application in the treatment of solid tumours.

Received 30th June 2025 Accepted 2nd August 2025

DOI: 10.1039/d5ra04640h

rsc.li/rsc-advances

Introduction

Dynamic covalent chemistry features chemical reactions that proceed reversibly under conditions governed by equilibrium-driven regulation. In these reactions, thermodynamic principles dictate product formation, ensuring that the product

"Engineering Research Centre of Tropical Medicine Innovation and Transformation of Ministry of Education, Key Laboratory of Tropical Translational Medicine of Ministry of Education, International Joint Research Centre of Human-Machine Intelligent Collaborative for Tumour Precision Diagnosis and Treatment of Hainan Province, Hainan Provincial Key Laboratory of Research and Development on Tropical Herbs, Haikou Key Laboratory of Li Nationality Medicine, School of Pharmacy, Hainan Medical University (Hainan Academy of Medical Science), Haikou, Hainan 571199, P. R. China. E-mail: maolujia@muhn.edu.cn

^bHainan Provincial Key Laboratory of Carcinogenesis and Intervention, School of Basic Medicine and Life Sciences, Hainan Medical University (Hainan Academy of Medical Science), Haikou, Hainan 571199, P. R. China

'Hainan Provincial Key Laboratory for Tropical Cardiovascular Diseases Research, School of Public Health, Hainan Medical University (Hainan Academy of Medical Science), Haikou, Hainan 571199, P. R. China

^aAffiliated Haikou Hospital of Xiangya Medical College, Central South University, P. R. China

† Those authors contributed equally.

distribution depends dominantly on the relative stabilities of the final compounds. The 1,3-diol skeleton is proved to be capable of binding with boronic acids followed by the formation of dioxaborinanes, which could potentially serve as a novel pH-responsive framework.²⁻⁴ Consequently, we employed andrographolide bearing the 1,3-diol moiety in the construction of dual drug delivery system for boron-containing drugs.⁵

Bortezomib (BTZ, Velcade®, Scheme 1A) acts on the mammalian 26S proteasome and inhibits nuclear factor-kappa B (NF-κB) signalling pathways.⁶ However, it is hindered by unfavourable pharmacokinetic properties, notably its poor solubility, rapid clearance from the bloodstream, and nonspecific binding to plasma proteins, which collectively limit its effectiveness in treating multiple myeloma (MM).⁷ Furthermore, systemic administration of BTZ is associated with side effects, including peripheral neuropathy, thrombocytopenia, and cardiotoxicity.⁸ To minimize the side effects, researchers have designed various strategies to improve the water solubility and stability of BTZ.⁹

Andrographolide (AND, Scheme 1B), a diterpenoid lactone, is a key phytochemical constituent of *Andrographis paniculata* and exhibits a spectrum of therapeutic effects, including anti-

Scheme 1 Crystal and molecular structure. (A) BTZ, (B) AND, (C) BSA and (D) BTZ-AND.

tumour activity. ¹⁰ Moreover, AND has been shown to inhibit the NF- κ B signalling pathway, indicating the potential for combination therapy with BTZ to achieve synergistic anti-cancer outcomes. ¹¹ However, AND has not yet attained its full therapeutic potential due to its poor water solubility (3.29 μ g mL $^{-1}$), which restricts its bioavailability. ¹² The protocol to improve the solubility of a molecule involves reducing its particle size through micronization or nanonization, thereby increasing its surface area and enhancing dissolution. ¹³

Albumin facilitates macropinocytosis-mediated catabolism in cancer cells, highlighting its potential as a carrier to improve the delivery of anti-cancer drugs into tumour cells.14,15 Among the various health-promoting protein-based delivery systems, bovine serum albumin nanoparticles (BSA NPs) stand out due to their non-toxic, biodegradable, biocompatible nature, high drug-binding capacity, significant accumulation at the tumour site, and convenient administration via injection (Scheme 1C).16 Additionally, AND, which possesses a 1,3-diol skeleton, acts as the binding site for BTZ through covalent interaction, leading to the formation of a six-member ring boronic ester known as BTZ-AND (Scheme 1D). Given that the BTZ-AND exhibited antitumour effects against U251 glioma cells and A549 cells, we conducted a spectroscopic investigation to explore the feasibility of delivering the covalent complex BTZ-AND with BSA NPs. Then, we developed the protocol to prepare the BTZ-AND@BSA NPs. Our findings offer an alternative way for the development of the dual drug delivery systems.

Results and discussion

The investigation of BTZ-AND formation *via* NMR measurements

The peaks at 5.07 ppm and 4.14 ppm in the 1 H NMR spectra of AND represent C1-OH and C2-OH, respectively (Fig. S1). 17 Upon the addition of BTZ to AND (1:1 ratio) in DMSO- d_6 , those two peaks significantly decreased, which suggested BTZ readily reacted with AND at room temperature (Fig. 1A). The formation

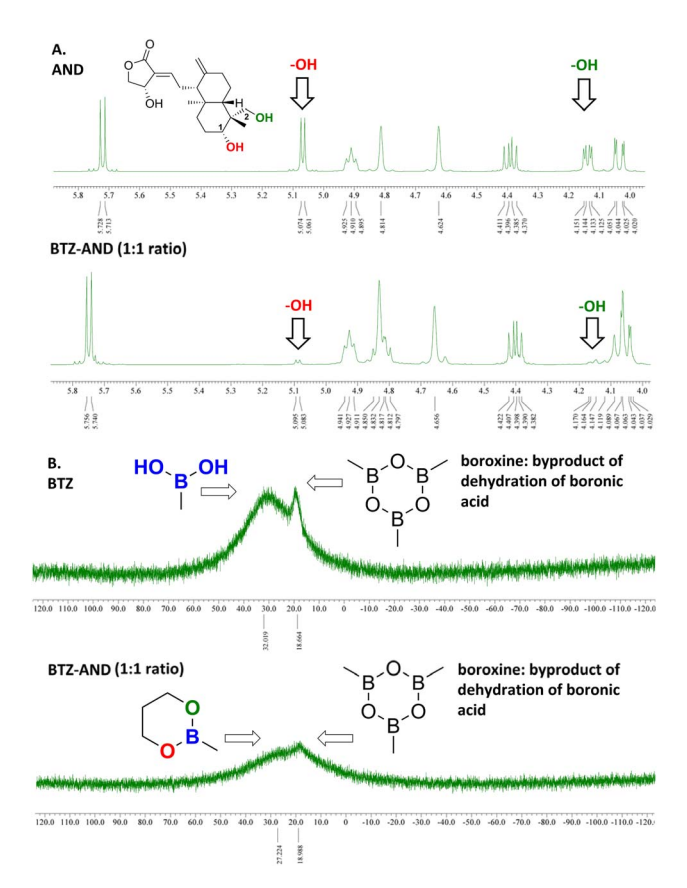


Fig. 1 NMR spectra of crude mixture BTZ-AND (1:1 ratio) in DMSO- d_6 at 25 °C. (A) 1 H NMR; (B) 11 B NMR.

of boronate esters were further approved by 11 B NMR measurements, where the peaks represent the boron atom in BTZ shifted from 32.02 ppm to 27.22 ppm (boron atom in BTZ-AND) (Fig. 1B). 18 The 1 H and 11 B NMR spectra suggested the formation of the six-member ring boronic ester BTZ-AND via the interaction of the 1,3-diol moiety with the boronic acid skeleton. Additionally, the BTZ-AND complex exhibited excellent stability. The 1 H and 11 B NMR spectra revealed that no significant decomposition occurred when the complex stored in DMSO- d_6 at room temperature for 24 h (Fig. 2).

Effects of the BTZ-AND complex on U251 glioma cells and A549 cells

The anti-tumour effects of the BTZ-AND complex on U251 and A549 cells are depicted in Fig. 3. The CCK-8 assay showed that the BTZ-AND complex (1 $\mu mol~L^{-1}$) had a significantly different effect on the survival rate of both U251 and A549 cells in comparison with the control groups. The fact that the BTZ-AND complex exhibited an inhibitory effect similar as BTZ alone suggests that the conjugation of AND does not compromise the anti-tumour efficacy of BTZ. This finding supports the potential of the BTZ-AND complex as a viable therapeutic agent, warranting further investigation into its mechanisms and in~vivo performance.

Paper

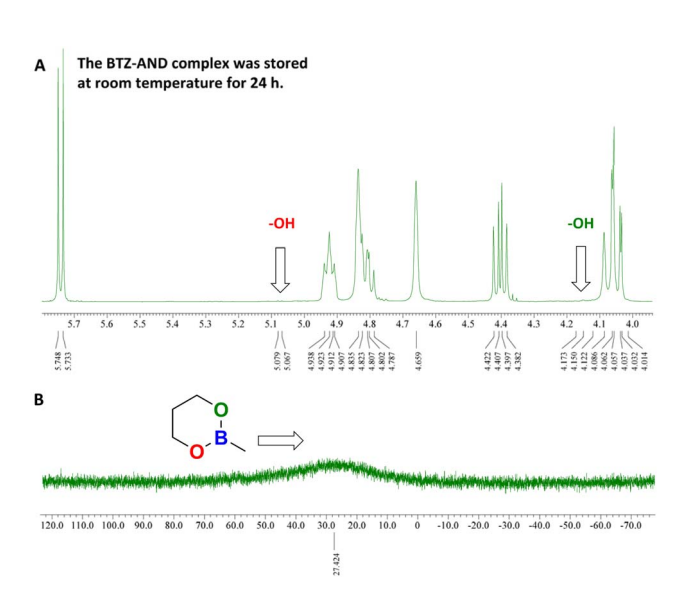


Fig. 2 NMR spectra of BTZ-AND complex in DMSO- d_6 . (A) $^1\mathrm{H}$ NMR; (B) $^{11}\mathrm{B}$ NMR.

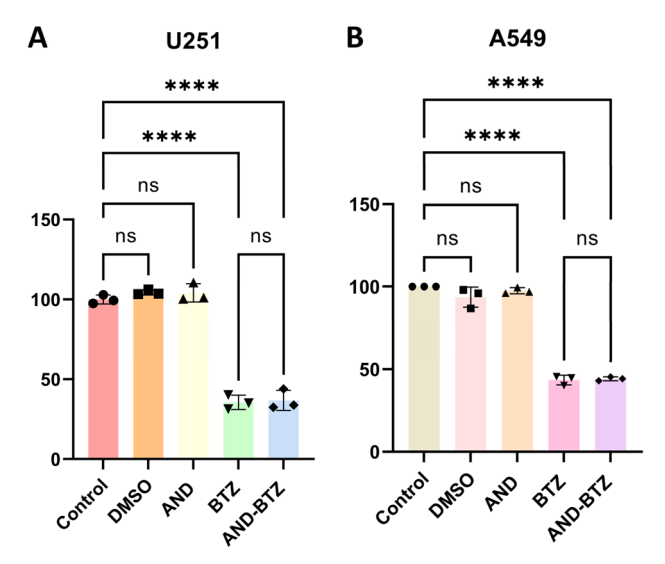


Fig. 3 The CCK-8 assay was used to assess cell viability for BTZ-AND after treatment with different dosages of the compound. These concentrations include 1 μ mol L $^{-1}$ BTZ-AND, 1 μ mol L $^{-1}$ AND, 1 μ mol L $^{-1}$ BTZ, and a 2% (v/v) DMSO solution. **** (ρ < 0.0001) denotes significant differences between groups and controls. U251 (A); A549 (B).

Determination of drug-BSA interaction *via* fluorescence spectra

The intrinsic fluorescence of BSA is primarily attributed to the presence of tryptophan (Trp), tyrosine (Tyr), and phenylalanine (Phe) residues. ¹⁹ As reported in previous studies, the fluorescence properties of BSA can undergo alterations upon binding to a ligand. ²⁰ The peak at 339 nm shown in the emission spectrum of BSA is a result of the Trp and Tyr residues presenting within its structure. When increasing concentrations of AND were added, the BSA fluorescence was only slightly quenched.

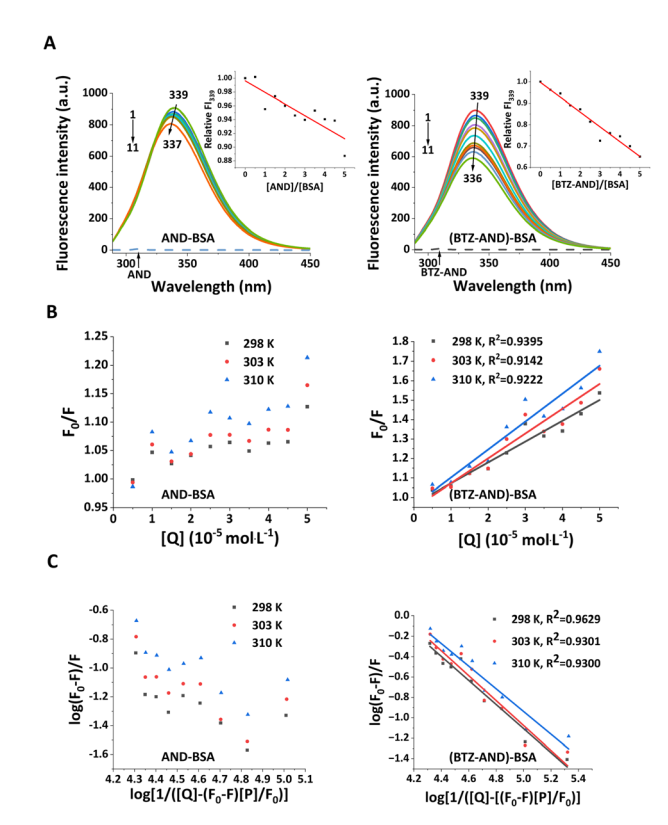


Fig. 4 (A) Fluorescence emission spectra of BSA (5 μ mol L⁻¹) in the presence of increasing concentrations of the drugs obtained at 25 °C, pH 7.4. The concentration of the drugs from spectra 1–11 was 0, 5, 10, 15, 20, 25, 30, 35, 40, 45, and 50 μ mol L⁻¹, respectively. The dashed lines show the fluorescence spectra of AND and BTZ-AND, respectively. The inset reveals that fluorescence of BSA at 339 nm (Fl_{339 nm}) drops as the drug is added relative to BSA. (B) Stern–Volmer plots for the fluorescence quenching of BSA induced by the drugs across a range of temperatures. (C) Double logarithmic plots for the temperature-dependent fluorescence quenching of BSA induced by the drugs.

When increasing concentrations of BTZ-AND were added, a significant quenching effect on the BSA fluorescence was observed. Notably, AND and BTZ-AND did not exhibit any fluorescence within this spectral range (the dashed lines at the bottom in Fig. 4A). At the highest concentration of AND (50 $\mu mol\ L^{-1}$), only 11% reduction in fluorescence intensity was observed (as shown in the inset of Fig. 4A, left). When it comes to BTZ-AND (50 $\mu mol\ L^{-1}$), an obvious 35% reduction in fluorescence intensity (as shown in the inset of Fig. 4A, right), indicating the stronger interaction of BTZ-AND with BSA than that of AND. 21

Fig. 4B and C (left) are lack of a discernible quenching pattern in the AND-BSA system suggesting minimal or nonspecific binding interactions. The data were collected at 298 K, 303 K, and 310 K using eqn (2) (see Materials and methods). The $K_{\rm SV}$ values for the (BTZ-AND)-BSA system, calculated from linear regression of the plots (Fig. 4B, right), are shown in Table 1. This distinction underscores stronger and more specific affinity of BTZ-AND towards BSA, likely due to structural features facilitating targeted binding.

Table 1 The quenching constant (K_{SV}) , biomolecular quenching rate constant (K_q) , and binding constants (K_a) for (BTZ-AND)-BSA interaction at three different temperatures, pH 7.4

T(K)	$K_{\rm SV} \left({ m L~mol^{-1}} \right)$	$k_{\mathrm{q}}~(\mathrm{L~mol^{-1}~s^{-1}})$	$K_{\rm a} ({ m L \; mol^{-1}})$
298 303 310	1.07×10^4 1.28×10^4 1.44×10^4	1.78×10^{12} 2.13×10^{12} 2.40×10^{12}	1.16×10^4 1.32×10^4 1.43×10^4

Table 2 The thermodynamic parameters for (BTZ-AND)-BSA interaction at three different temperatures, pH 7.4

<i>T</i> (K)	ΔH (kJ mol ⁻¹)	ΔS (J mol ⁻¹ K ⁻¹)	ΔG (kJ mol ⁻¹)
298 303 310	+19.41	+177.53	-33.50 -34.38 -35.63

The $k_{\rm q}$ values in Table 1 for the (BTZ-AND)-BSA system were much higher than the maximum quenching constant of 2 \times 10¹⁰ L mol⁻¹ s⁻¹, which is usually seen for interactions between quenchers and the fluorophore in a bimolecular complex.²² Binding BSA to BTZ-AND likely induced fluorescence quenching, forming a stable (BTZ-AND)-BSA complex.

Table 1 lists the binding constants (K_a) of BTZ-AND to BSA at pH 7.4 and different temperatures. The double-logarithmic plots for these data are in Fig. 4C (right).²³ The K_a values for the (BTZ-AND)-BSA system were between 1.16 \times 10⁴ and 1.43 \times 10⁴ L mol⁻¹, showing a moderate binding affinity between BTZ-AND and BSA.²⁴ The temperature-dependent increase in K_a further suggests that the (BTZ-AND)-BSA complex remains stable during blood circulation, which is crucial for maintaining therapeutic efficacy *in vivo*. These findings align with the requirements for effective drug delivery systems, where moderate protein binding ensures prolonged circulation without compromising bioavailability.

The determination of thermodynamic parameters, including ΔH , ΔS , and ΔG , for the (BTZ-AND)-BSA interaction are crucial for identifying the forces that drive the binding process. Table 2 presents the values of ΔH and ΔS , along with the ΔG values determined at three distinct temperatures. Although the positive ΔH indicates that the formation of the (BTZ-AND)-BSA complex is an endothermic reaction, the value of ΔG is negative, implying that the binding interaction occurs spontaneously across all temperatures. Given that both ΔH and ΔS values are positive, obtained for the (BTZ-AND)-BSA system, it suggests that hydrophobic interactions play a significant role in stabilizing the (BTZ-AND)-BSA complex. Section 1.25

Three-dimensional fluorescence spectra

The analysis of the 3-D fluorescence spectra of BSA in the presence of the drug reveals perturbations in the microenvironment surrounding the Tyr and Trp residues of BSA, which are caused by the binding of the drugs.²⁷ Fig. 5 presents the 3-D fluorescence spectra and their corresponding contour maps for

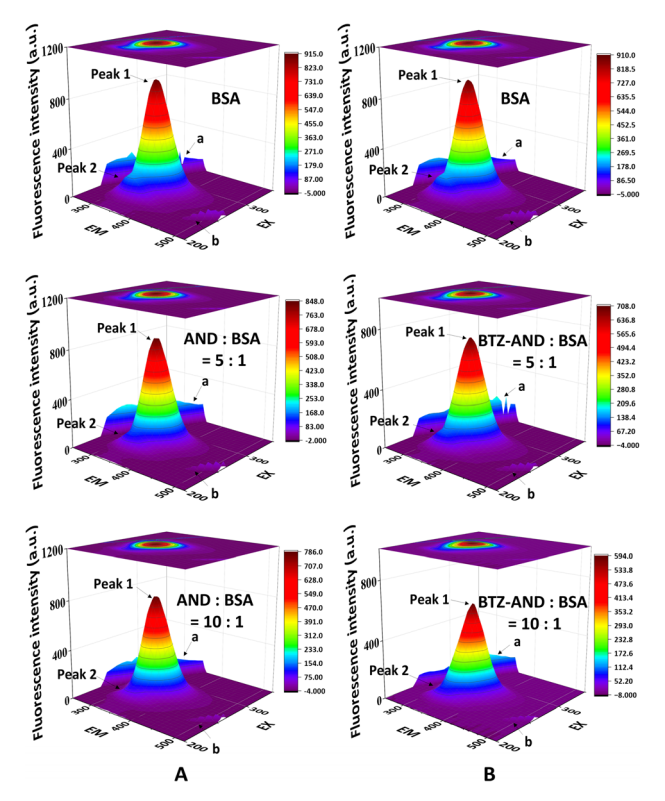


Fig. 5 (A) The 3-D fluorescence spectra of BSA (5 μ mol L⁻¹), AND-BSA (5:1) and AND-BSA (10:1) systems at 25 °C, pH 7.4. (B) The 3-D fluorescence spectra of BSA (5 μ mol L⁻¹), (BTZ-AND)-BSA (5:1) and (BTZ-AND)-BSA (10:1) systems at 25 °C, pH 7.4.

BSA, AND-BSA, and (BTZ-AND)-BSA systems. The spectral data for these systems are summarized in Tables 3 and S1. The 3-D fluorescence spectrum of BSA usually shows four peaks. The first-order Rayleigh scattering peak ($\lambda_{ex} = \lambda_{em}$) and the secondorder Rayleigh scattering peak $(2\lambda_{ex} = \lambda_{em})$ are labeled as peaks 'a' and 'b'.28 Peak 1 primarily arises from the fluorescence emission of tryptophan (Trp) and tyrosine (Tyr) residues.29 Peak 2 is predominantly governed by the fluorescence spectral features of the polypeptide backbone conformation. The peak intensities are directly correlated with the microenvironmental conditions of the protein.30 Upon comparing the 3-D fluorescence spectra of BSA in the absence and presence of a 5-fold molar excess of AND, only marginal intensity reductions were noted as peak 1 exhibited about 6% decrease and peak 2 showed about 28% reduction (Fig. 5A and Table S1). When a 10 molar excess of AND is present, the 3-D fluorescence spectra did not exhibit great alternations. Upon conducting a comparative assessment of the 3-D fluorescence spectra of BSA in the absence and presence of a 5-fold molar excess of BTZ-AND, marginal intensity alterations were identified as peak 1 exhibited about 20% decline and peak 2 displayed about 34% reduction (Table 3). These alterations in the 3-D fluorescence spectra become even more pronounced when a 10 molar excess of BTZ-AND is present (Fig. 5B and Table 3). These alterations in the 3fluorescence spectra indicated microenvironmental

Table 3 3-D Fluorescence spectral data of BSA (5 µmol L⁻¹) and (BTZ-AND)-BSA complexes at 25 °C, pH 7.4

System	Peak	Peak position $\left[\lambda_{ex}/\lambda_{em} \left(nm/nm\right)\right]$	Intensity
BSA	a	$250/250 \rightarrow 350/350$	$163.01 \rightarrow 100.12$
	b	$235/470 \rightarrow 260/520$	$9.67 \to 56.76$
	1	280/339	883.46
	2	240/340	204.55
[BTZ-AND]:[BSA] = 5:1	a	$250/250 \rightarrow 350/350$	$116.54 \rightarrow 129.07$
	b	$235/470 \rightarrow 260/520$	$5.04 \rightarrow 39.49$
	1	280/339	705.30
	2	240/340	134.70
[BTZ-AND]:[BSA] = 10:1	a	$250/250 \rightarrow 350/350$	$70.95 \rightarrow 112.09$
	b	$235/470 \rightarrow 260/520$	$2.60 \to 26.35$
	1	280/335	561.71
	2	240/335	89.43

perturbations around the Trp and Tyr residues, thereby suggesting a robust interaction between BTZ-AND and BSA.

UV-Vis absorption results

UV-Vis absorption spectroscopy is an easy way to study how proteins change structure and how they bind with ligands.³¹ To ascertain if the (BTZ-AND)-BSA complex formed or not, we recorded UV absorption spectra of BSA without (spectrum 1) and with (spectra 2–11) increasing amounts of BTZ-AND (Fig. 6A). To ensure how the UV absorption spectra of BSA changed with different BTZ-AND amounts, we subtracted the spectra of free BTZ-AND (Fig. S7) from those of the (BTZ-AND)-BSA complex. BSA has two distinct absorption peaks. The peak at 220 nm shows changes in the structure of BSA's peptide

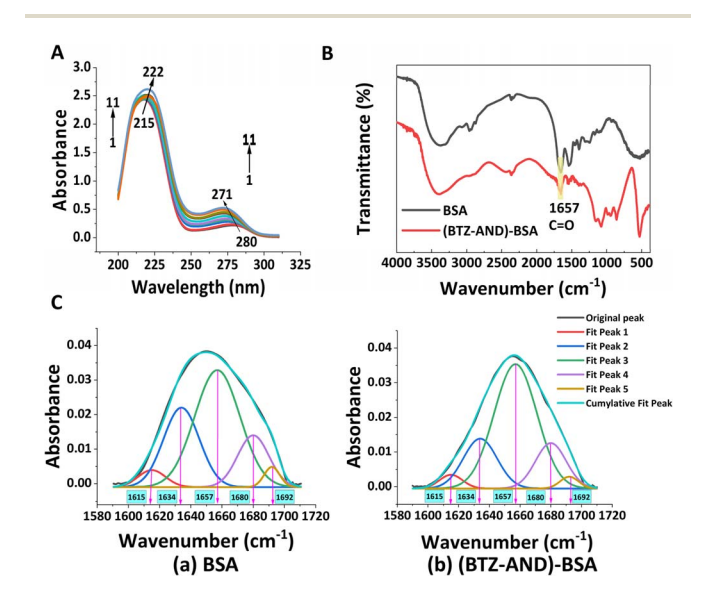


Fig. 6 (A) UV-Vis absorption spectra of BSA (5 μmol L⁻¹), in the presence of increasing concentrations of BTZ-AND obtained at 25 °C, pH 7.4. The concentration of BTZ-AND from spectra 1–11 was 0, 5, 10, 15, 20, 25, 30, 35, 40, 45, and 50 μmol L⁻¹, respectively. (B) FT-IR spectra of BSA, obtained in the absence (black) and presence (red) of BTZ-AND. (C) FT-IR spectra of BSA subjected to second derivative resolution enhancement and curve-fitting of the amide I region (1600–1700 cm⁻¹) at room temperature. Free BSA (a); (BTZ-AND)-BSA (b).

backbone, while the peak at 280 nm comes from π – π and n– π * transitions in the aromatic heterocycles of Tyr, Trp, and Phe, as well as other chromophores in the protein chain. Remarkably, upon the addition of BTZ-AND, the absorption near 220 nm increased significantly, and the peak shifted from 215 nm to 222 nm. This suggests that the (BTZ-AND)-BSA complex changes the structure of BSA and affects its α -helix content. This observation further supports the notion that the fluorescence quenching arises predominantly from the efficient and specific binding of BTZ-AND to BSA, indicating a key interaction in the system.

FT-IR measurements

In our study, infrared spectroscopy and its derivative methodologies are employed to analyse conformational changes in BSA, offering significant insights through the observation of peak shifts and intensity variations within the amide I band of BSA (primarily due to C=O stretching).³³ The amide I band, located within the range of 1600–1700 cm⁻¹, is highly sensitive to subtle alterations in the secondary structures of proteins and is commonly utilized for the characterization of these secondary structures. However, we can measure the amount of secondary structure by calculating the area under the amide I peak.

To monitor how the amide I band changes and how the structure of BSA is affected by BTZ-AND, we measured FT-IR spectra of BSA without and with BTZ-AND, focusing on the C=O stretch (Fig. 6B). The FT-IR spectrum of native BSA (Fig. 6B) shows a strong peak at 1657 cm⁻¹ in the amide I region, suggesting that BSA mostly has an α -helix structure. However, the addition of BTZ-AND induced a measurable change in the spectral features of amide I band relative to native BSA, suggesting structural alterations. The observed changes are likely due to BTZ-AND binding to the C=O, C-N, and N-H groups of BSA, resulting in a reconfiguration of the hydrogen-bonding interactions within the polypeptide carbonyl backbone.

In BSA, hydrogen bonds between the carbonyl (C=O) and amide (N-H) groups in its peptide backbone keep its secondary structures stable. The positions and sizes of spectral peaks in the amide I band can provide us about how hydrogen bonds are arranged and how strong they are in protein secondary

Table 4 Proportions of secondary structures in BSA without and with BTZ-AND

Secondary structures	Free BSA	(BTZ-AND)-BSA
α-Helix (%)	50.19	59.58
β-Sheet (%)	4.43	3.54
β-Turn (%)	15.32	15.60
β-Antiparallel (%)	3.00	2.43
Random coil (%)	27.04	18.85

structures.³⁴ We analysed the secondary structures of free BSA and the (BTZ-AND)-BSA complex in detail employing FT-IR self-deconvolution, second-derivative resolution, and curve-fitting techniques. The outcomes of the analysis are presented in Fig. 6C and Table 4. The calculated results showed that free BSA was 50.19% α -helix (1657 cm⁻¹), 4.43% β -sheet (1615 cm⁻¹), 3.00% β -antiparallel (1692 cm⁻¹), 15.32% β -turn structure (1680 cm⁻¹), and 27.04% random coil (1634 cm⁻¹).³⁵ When BTZ-AND bound to BSA, the α -helix content rose from 50.19% (free BSA) to 59.58% (BTZ-AND-BSA). We also observed changes in other secondary structures, suggesting that some α -helix were reshaped into different forms, such as β -sheet, β -turn, β -antiparallel, and random coil structures.

Computational modelling analysis

We employed molecular docking to find the best pattern that the ligand binds to its target site, showing details at the atomic level.36 The energy of BTZ-AND was minimized as well as the geometry was optimized, and then the exploration of the configuration space encompassed within grid boxes, centred on BSA was carried out.³⁷ The optimized computed binding energy of BTZ-AND is -33.47 kJ mol⁻¹. The experimentally obtained binding energies fall within a similar range as those predicted by molecular docking, thus validating the results. Hydrophobic interactions through Lys-114, Lys-116, Pro-117, Tyr-160, Ile-181, Arg-185 and Pro-516 would be dominant in stabilizing the complex of (BTZ-AND)-BSA in proximity (Fig. 7, right). Hydrogen bonding through Leu-115, Tyr-160 and Arg-185 were also observed. Additionally, a salt bridge was also found between Lys-116 and BTZ-AND. The docking simulation suggested that BTZ-AND has a binding preference towards BSA, involving

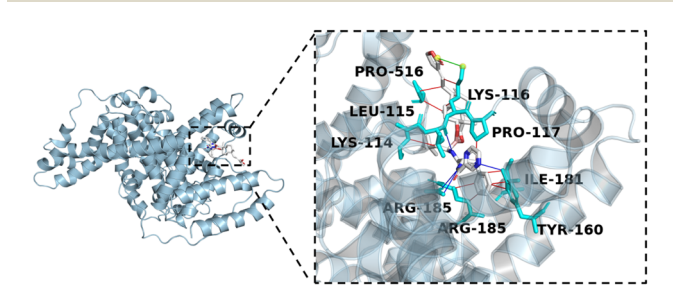


Fig. 7 Left: BTZ-AND (shown as sticks) binds to BSA in its lowestenergy conformation. Right: zoomed-in view of the binding site, showing hydrophobic interactions (red lines), hydrogen bonds (blue lines), and a salt bridge (green line).

hydrophobic interactions, hydrogen bonds and a salt bridge in the (BTZ-AND)-BSA complex formation.

Optimization of the procedure for the preparation of nanoparticles

We employed the controlled desolvation technique to optimize the procedure for the preparation of BTZ-AND@BSA NPs. ¹⁶ The procedure was optimized including water-to-ethanol ratio, drop

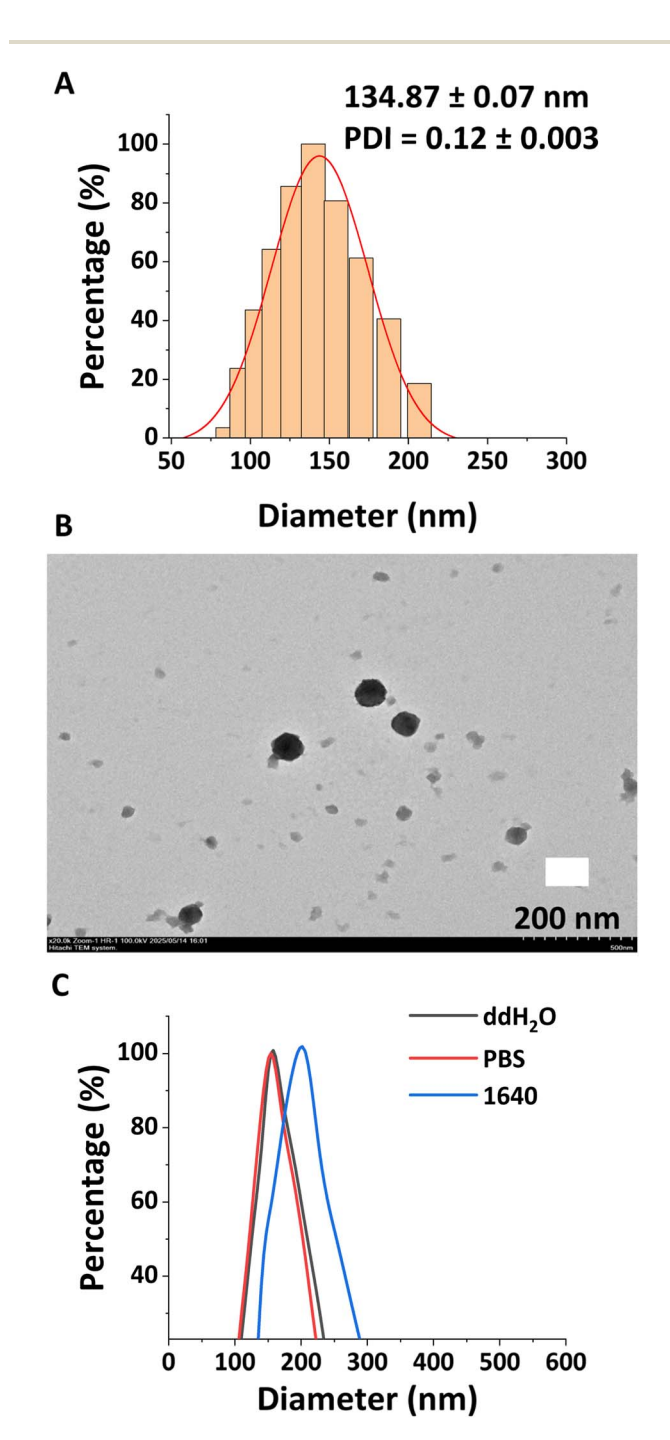


Fig. 8 (A) Particle size distribution of BTZ-AND@BSA NPs (n=3). (B) TEM image of BTZ-AND@BSA NPs. (C) Stability of BTZ-AND@BSA NPs (n=3).

Paper

rate of ethanol, pH, BSA concentration and time for crosslink (Tables S2-S6). With the optimized conditions in hands, BTZ-AND@BSA NPs were prepared. The particle size was 134.87 \pm 0.07 nm (Fig. 8A and B), and zeta potential was $-16.37 \pm$ 1.67 mV. The EE and DL of BTZ-AND@BSA NPs were 90.56% and 9.05%, respectively. The BTZ-AND@BSA NPs were incubated in deionized water, PBS (pH 7.4), and PRIM 1640 for 24 h, and the particle size were 160.15 \pm 4.79 nm (PDI: 0.14 \pm 0.003), 181.69 \pm 1.98 nm (PDI: 0.18 \pm 0.026) and 162.97 \pm 2.50 nm (PDI: 0.18 ± 0.009), respectively (Fig. 8C). It suggested that the nutrient in the biological cultivation environment did not affect significantly on the structure of BTZ-AND@BSA NPs.

The blue cell nuclei stained with DAPI were surrounded by clear green fluorescence signals, as seen in Fig. 9A and B. The Ce6@BSA NPs and Ce6@BTZ-AND@BSA NPs were employed for the in vitro cellular uptake investigation. The U251 cells and A549 cells were incubated with Ce6@BSA NPs or Ce6@BTZ-AND@BSA NPs for 12 h and the fluorescent images were recorded. The results suggested that BSA NPs could be absorbed by U251 cells and A549 cells efficiently, which proved the possibility to deliver BTZ-AND with BSA NPs for the treatment of glioma and lung cancers.

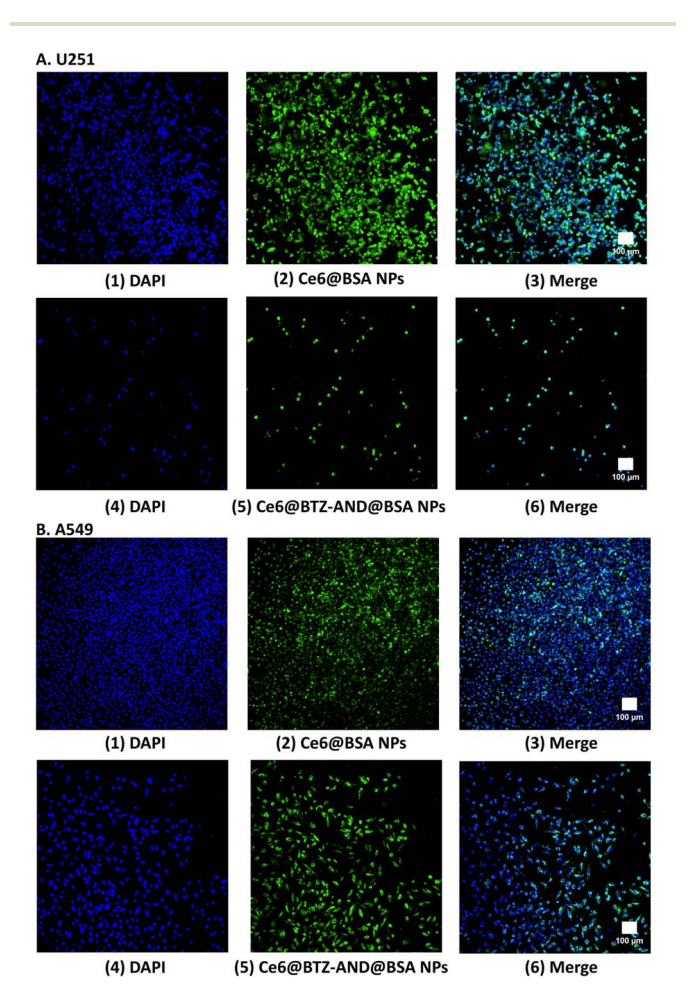


Fig. 9 (A) Fluorescent images of U251 glioma cells incubated under different conditions for 12 h (n=3). (B) Fluorescent images of A549 cells incubated under different conditions for 12 h (n = 3).

Conclusions

The investigation of NMR spectra revealed that the covalent interaction induced the formation of BTZ-AND, which exhibited similar anti-tumour effects as BTZ against both U251 glioma cells and A549 cells. Furthermore, the reorganization of boronic acids towards 1,3-diols has significant application in tumour targeting and transcellular transfer. The molecular characterization of BTZ-AND binding to BSA was conducted, yielding a binding affinity of $K_a = 1.16 \times 10^4 \text{ L mol}^{-1}$ at 25 °C. Both experimental and molecular docking studies revealed that hydrophobic interactions are the major factors in stabilizing (BTZ-AND)-BSA complex. Three-dimensional fluorescence and FT-IR measurements showed that the binding of BTZ-AND altered secondary structures of BSA and changed the environment around its fluorophores. Based on these results, the BTZ-AND@BSA NPs were prepared and properly characterized. These observations provided comprehensive insights into the binding properties of BTZ-AND to BSA, potentially paving the way for future medical and pharmaceutical applications.

Materials and methods

Materials

Bortezomib, andrographolide, bovine serum albumin, 25% glutaraldehyde, ethanol, sodium phosphate dihydrate and sodium phosphate dibasic dodecahydrate were purchased from Energy Chemical Co., Ltd, and used without further purification. All other reagents were of analytical grade. The U251 was obtained by a general donation from Prof. Zhaohui Liu (Hainan Medical University Hainan Hospital) and the A549 was purchased from Procell Life Science & Technology.

Methods

Sample preparation. BSA (1.25 mmol) was dissolved in 60 mmol L^{-1} sodium phosphate buffer at pH 7.4. The stock solutions (0.5 mmol L^{-1}) of AND and BTZ-AND (1:1 ratio) were prepared by dissolving their solids in ethanol, respectively. The stock solution was diluted to the target concentration using the designated buffer for experimental use.

¹H- and ¹¹B-NMR measurements. All NMR spectra were recorded at ambient temperature using a JEOL JNM-ECZ400S/L NMR (¹H, 400 MHz; ¹¹B, 128 MHz) spectrometer. ¹H NMR chemical shifts are reported relative to TMS and were referenced via residual proton resonances of the corresponding deuterated solvent (DMSO-d₆: 2.50 ppm). ¹¹B NMR chemical shifts are quoted relative to BF₃·Et₂O as external standard.

The BTZ-AND sample was prepared upon the addition of AND (22.8 mg, 1 equiv.) into DMSO- d_6 (0.5 mL) containing BTZ (25.0 mg, 1 equiv.) and stirred vigorously for 2 h at room temperature.

CCK-8 assay. U251 and A549 cells were divided into 96-well plates, each containing 1×10^4 cells, and incubated for the entire night using the CCK-8 test to measure their rate of proliferation. The supernatant was aspirated after 48 hours of treatment with different doses of BTZ, AND, and BTZ-AND (1

RSC Advances

 μ mol L⁻¹). Each well was then filled with 100 μ L of DMEM that contained 10% FBS and was combined with 10% CCK-8 solution (C0039, Beyotime Biotech Inc.). The cells were then incubated for 90 minutes at 37 °C. A microplate reader (BioTek Instruments Inc.) quantified the optical density (OD) at 450 nm. The results are expressed as the mean \pm standard error of the mean (SEM), with statistical analyses conducted using Graph-Pad Prism software (version 9.5, USA-developed). A one-way ANOVA, which can be parametric or nonparametric, was conducted based on the homogeneity of variances across the groups. Post hoc tests were then used where it was thought suitable. Statistical significance was defined as a P-value < 0.05.

UV spectroscopy. UV spectra were recorded using a UV-Vis spectrophotometer (PGeneral T6) over the wavelength range of 190-310 nm, with a bovine serum albumin (BSA) concentration of 5 μmol L⁻¹. UV spectra of BSA were measured with increasing BTZ-AND concentrations (5-50 μ mol L⁻¹, in 5 μ mol L⁻¹ increments), along with UV spectra of BTZ-AND solutions at the same concentrations.

Fluorescence spectroscopy. Fluorescence spectra were recorded using a Hitachi F-4700 spectrofluorometer at three defined temperatures (298 K, 303 K, and 310 K), with temperature stability ensured by a dedicated temperature controller. The samples were excited at 280 nm, and the emission spectra of the AND-BSA or (BTZ-AND)-BSA complexes were acquired across the wavelength range of 290-450 nm at a scanning rate of 1200 nm min⁻¹. The bandwidths for excitation and emission were set to 5 nm. All reported data represent the average of three independent measurements.

Three-dimensional (3-D)fluorescence spectra measured for bovine serum albumin (BSA) at 5 μ mol L⁻¹, both in its native state and after the addition of the drug at molar ratios of 5:1 and 10:1 (ligand: BSA). The excitation wavelength was scanned from 220 nm to 350 nm in 5 nm increments, while the emission wavelength was continuously recorded over the 220 nm to 500 nm range.

Fluorescence quenching experiments were conducted to investigate the effect of the drug on BSA. BSA concentration was maintained at 5 µmol L⁻¹, and the drug concentrations were systematically increased from 5 μ mol L⁻¹ to 50 μ mol L⁻¹. Fluorescence spectra of bovine serum albumin (BSA) were recorded at three distinct temperatures: 298 K, 303 K, and 310

To avoid the inner filter effect, the fluorescence intensity was corrected using eqn (1):

$$F_{\rm cor} = F_{\rm obs} e^{(A_{\rm ex} + A_{\rm em})/2}$$
 (1)

where F_{cor} is the corrected fluorescence intensity, and F_{obs} is the observed intensity; $A_{\rm ex}$ and $A_{\rm em}$ are the absorbance values of BSA (with the drug) at the excitation and peak emission wavelengths, respectively.

We analysed the corrected fluorescence data to study the quenching mechanism with the Stern-Volmer equation:

$$F_0/F = 1 + K_{SV}[Q] = 1 + k_0 \tau_0[Q]$$
 (2)

where F_0 is the fluorescence intensity of BSA without the drug, and F is the intensity with the drug; [Q] is the concentration of the drug, and K_{SV} is the Stern-Volmer constant.

The $k_{\rm q}$ refers to bimolecular quenching rate constant:

$$k_{\rm g} = K_{\rm SV}/\tau_0 \tag{3}$$

where τ_0 is the average lifetime of BSA, which was taken as 6 \times 10^{-9} s for BSA.

The drug quenched the fluorescence of BSA as it formed a non-fluorescent complex with BSA. Eqn (4) describes how the drug affects the fluorescence intensity of BSA:

$$\log(F_0 - F)/F = n \log K_a - n \log[1/([Q] - (F_0 - F)[P]/F_0)]$$
 (4)

where F_0 is the fluorescence intensity of BSA without the drug, and F is the intensity with the drug; K_a is the binding constant, nis the number of binding sites, [Q] is the total concentration of the drug, and [P] is the total concentration of BSA.

To assess the key factor contributing to the stability of the (BTZ-AND)-BSA complex, thermodynamic parameters (ΔH , ΔS , and ΔG) were obtained through analysis of the van't Hoff and Gibbs-Helmholtz equations:

$$\ln K_{\rm a} = -\Delta H/RT + \Delta S/R \tag{5}$$

$$\Delta G = \Delta H - T \Delta S \tag{6}$$

where R is the gas constant (8.314 J mol^{-1} K^{-1}), and T is the absolute temperature (298, 303, or 310 K); ΔH is the enthalpy change, ΔS is the entropy change, and ΔG is the Gibbs free energy change.

FT-IR measurements. FT-IR measurements were carried out at room temperature using a Nicolet iS5 spectrometer. We averaged 16 scans to get each spectrum, with a resolution of 0.4 cm⁻¹. First, we recorded the FT-IR spectra of BSA without and with BTZ-AND, from 400 cm⁻¹ to 4000 cm⁻¹. The secondary structure content of the amide I region (v 1600–1700 cm⁻¹) was deconvoluted by second derivative.

Molecular docking studies. We employed molecular docking to get a better understand how BSA and BTZ-AND interact. The BSA structure (PDB ID: 4F5S) was downloaded from the RCSB Protein Data Bank (https://www.rcsb.org/pdb). The structure of BSA was optimized and water molecules in the BSA were deleted. The computationally predicted binding sites between BSA and BTZ-AND were established using AutoDock 4.2 (developed by the Scripps Research Institute Molecular Graphics Laboratory, La Jolla, CA, USA). Among the docking poses, the one with the most favorable docking energy (highest score) was designated as the optimal model. The docking results were visualized and analyzed using PyMOL (version 1.3r1, DeLano Scientific LLC, South San Francisco, CA, USA).

Procedure for the preparation and characterization of BTZ-AND@BSA NPs. The BTZ-AND@BSA NPs were prepared utilizing a controlled desolvation technique. 16 BTZ (15.8 mg) and AND (17.5 mg) were dissolved in EtOH (10.00 mL) and stirred for 2 h. Then, BTZ-AND was obtained after the solvent was removed by rotate evaporation. BTZ-AND was re-dissolved

Paper RSC Advances

in EtOH (3.00 mL), and the pH was adjusted to 9 using 1 mol L^{-1} NaOH. EtOH (11.50 mL) was added dropwise (1 mL min⁻¹) into 2% BSA (pH 9) followed by the addition of BTZ-AND solution, and then stirred for 30 min. Upon the addition of 25% glutaraldehyde (16.8 µL), the mixture was stirred for another 8 h. To procure the crude BTZ-AND@BSA NPs, the solvent was evaporated to 1 mL, followed by centrifugation at 14 000 rpm. The obtained crude NPs were then dissolved in water, and the final product was obtained after freeze-drying. The Ce6@BSA NPs and Ce6@BTZ-AND@BSA NPs were prepared via a similar procedure. The particle size, zeta potential and polydispersity index (PDI) were measured on a Zeta sizer Nano-1900 (Malvern Instruments, USA). Transmission electron microscopy (TEM) was recorded on a Hitachi HT7800 microscope. The fluorescent images were recorded on the laser scanning confocal microscope. The encapsulation efficiency (EE) and drug loading (DL) were calculated by analysing BTZ-AND via UV-Vis spectroscopy. EE (%) = (amount of loaded drug/amount of added drug) \times 100 and DL (%) = (amount of loaded drug/weight of NPs) \times 100.

Cellular uptake. The U251 and A549 cells were seeded onto confocal-specific cell culture dishes and then incubated overnight at 37 °C with 5% CO₂ in an incubator maintained at a constant temperature until they stuck to the wall and proliferated properly. The first culture media was removed and replaced with fresh culture medium containing Ce6@BSA NPs or Ce6@BTZ-AND@BSA NPs. The cells were continually cultured for 12 hours in order to allow the nanoparticles to fully interact with them. After the cell nuclei were labelled with DAPI nuclear dye, the uptake of the nanoparticles by the cells and their intracellular distribution characteristics were observed using a confocal laser scanning microscope (CLSM).

Author contributions

S. Qiao: investigation, methodology, formal analysis, writing – original draft; H. Long: methodology, for-mal analysis; Y. Song: investigation, methodology, supervision; X. Dong: formal analysis, supervision; H. Zhong: formal analysis; H. Meng: formal analysis; J. Gong: data curation, formal analysis; Y. Wang: data curation; Y. Liu: conceptualization, supervision; H. Zhang: conceptualization, supervision, writing – review & editing; L. Mao: conceptualization, project administration, supervision, writing – review & editing.

Conflicts of interest

There are no conflicts to declare.

Data availability

All data are contained in the manuscript and SI. Supplementary information is available. See DOI: https://doi.org/10.1039/d5ra04640h.

Acknowledgements

L. M. thanks Hainan Provincial Natural Science Foundation of China (project number: 222RC680) and start-up research grant (XRC200014, Hainan Medical University) for funding. H. Z. thanks Hainan Province Science and Technology Special Fund of China (project number: ZDYF2022SHFZ290) and Academic Enhancement Support Program of Hainan Medical University (project number: XSTS2025125) for funding.

Notes and references

- 1 S. J. Rowan, S. J. Cantrill, G. R. L. Cousins, J. K. M. Sanders and J. F. Stoddart, *Angew. Chem., Int. Ed.*, 2002, 41, 898–952.
- 2 L. Dai, J. Liu, T. Yang, X. Yu, Y. Lu, L. Pan, S. Zhou, D. Shu, Y. Liu, W. Mao and Z. Qian, *Nat. Commun.*, 2025, **16**, 1329.
- 3 A. Stubelius, S. Lee and A. Almutairi, *Acc. Chem. Res.*, 2019, **52**, 3108–3119.
- 4 H. Liu, Y. Li, K. Sun, J. Fan, P. Zhang, J. Meng, S. Wang and L. Jiang, J. Am. Chem. Soc., 2013, 135, 7603–7609.
- 5 Y. Dai, S.-R. Chen, L. Chai, J. Zhao, Y. Wang and Y. Wang, Crit. Rev. Food Sci., 2019, 59, S17–S29.
- 6 P. Sonneveld, M. A. Dimopoulos, M. Boccadoro, H. Quach, P. J. Ho, M. Beksac, C. Hulin, E. Antonioli, X. Leleu,
- S. Mangiacavalli, A. Perrot, M. Cavo, A. Belotti, A. Broijl,
- F. Gay, R. Mina, I. S. Nijhof, N. W. C. J. Van De Donk,
- E. Katodritou, F. Schjesvold, A. Sureda Balari, L. Rosiñol,
- M. Delforge, W. Roeloffzen, T. Silzle, A. Vangsted,
- H. Einsele, A. Spencer, R. Hajek, A. Jurczyszyn,
- S. Lonergan, T. Ahmadi, Y. Liu, J. Wang, D. Vieyra, E. M. J. Van Brummelen, V. Vanquickelberghe, A. Sitthi-Amorn, C. J. De Boer, R. Carson, P. Rodriguez-Otero,
- J. Bladé and P. Moreau, N. Engl. J. Med., 2024, 390, 301-313.
- 7 C. R. C. Tan, S. Abdul-Majeed, B. Cael and S. K. Barta, *Clin. Pharmacokinet.*, 2019, 58, 157–168.
- 8 G. Cengiz Seval and M. Beksac, Expert Opin. Drug Saf., 2018, 17, 953-962.
- 9 J. Liu, R. Zhao, X. Jiang, Z. Li and B. Zhang, *Biomolecules*, 2022, **12**, 51.
- 10 P. Agrawal and M. S. Nair, Fund. Clin. Pharmacol., 2022, 36, 586–600.
- 11 J. Hu, Y. Li, X. Xie, Y. Song, W. Yan, Y. Luo and Y. Jiang, *Biomed. Pharmacother.*, 2024, **180**, 117438.
- 12 B. Zeng, A. Wei, Q. Zhou, M. Yuan, K. Lei, Y. Liu, J. Song, L. Guo and Q. Ye, *Phytother. Res.*, 2022, **36**, 336–364.
- 13 R. Deshmukh, A. K. Jain, R. Singh, S. D. Paul and R. K. Harwansh, *Curr. Drug Deliv.*, 2024, **21**, 631–644.
- 14 A. O. Elzoghby, W. M. Samy and N. A. Elgindy, *J. Contr. Release*, 2012, **157**, 168–182.
- 15 S. Shrestha, A. Shrestha, J. Kim, R. K. Thapa and J. O. Kim, *J. Pharm. Investig.*, 2025, 55, 1–14.
- 16 X. Xu, J. Hu, H. Xue, Y. Hu, Y. Liu, G. Lin, L. Liu and R. Xu, Int. J. Biol. Macromol., 2023, 253, 126914.
- 17 J. Vilvest, M. C. J. Milton, A. Yagoo and K. Balakrishna, *Exp. Parasitol.*, 2024, **267**, 108858.
- 18 A. J. Howarth, T. C. Wang, S. S. Al-Juaid, S. G. Aziz, J. T. Hupp and O. K. Farha, *Dalton Trans.*, 2016, **45**, 93–97.

- 19 Y. Guo, J. Tong, Y. Guo, X. Song, K. Shi, Z. Guo, B. Liu and J. Xu, *Food Hydrocoll.*, 2025, **160**, 110836.
- 20 B. Wu, J. Wang, Y. Chen and Y. Fu, ACS Biomater. Sci. Eng., 2024, 10, 743–761.
- 21 D. M. Makanyane, S. Maikoo, F. R. Van Heerden, L. Rhyman, P. Ramasami, L. P. Mabuza, P. Ngubane, A. Khathi, A. Mambanda and I. N. Booysen, *J. Inorg. Biochem.*, 2024, 255, 112541.
- 22 W. R. Ware, J. Phys. Chem., 1962, 66, 455-458.
- 23 S.-B. Kou, Z.-Y. Lin, B.-L. Wang, J.-H. Shi and Y.-X. Liu, *J. Mol. Struct.*, 2021, **1224**, 129024.
- 24 S. Fan, Z. Lu, Z. Yan and L. Hu, *Int. J. Biol. Macromol.*, 2024, 274, 133370.
- 25 E. Yadollahi, B. Shareghi and S. Farhadian, *J. Mol. Liq.*, 2022, **353**, 118826.
- 26 A. Jalan, S. Sangeet, A. K. Pradhan and N. S. Moyon, *J. Mol. Recognit.*, 2024, 37, e3084.
- 27 L. Wang, X. Wu, Z. Zhao, F. Fan, M. Zhu, Y. Wang, R. Na and Q. X. Li, J. Agric. Food Chem., 2020, 68, 2329–2339.
- 28 M. Z. Kabir, J. Seng, S. B. Mohamad, M. Gülsüm Bilgiç and B. Uslu, *J. Photochem. Photobiol.*, A, 2024, **450**, 115464.

- 29 M. Makarska-Bialokoz and A. Lipke, J. Mol. Liq., 2019, 276, 595–604.
- 30 F.-F. Tian, F.-L. Jiang, X.-L. Han, C. Xiang, Y.-S. Ge, J.-H. Li, Y. Zhang, R. Li, X.-L. Ding and Y. Liu, *J. Phys. Chem. B*, 2010, 114, 14842–14853.
- 31 Z.-L. Zang, Y.-X. Wang, N. Battini, W.-W. Gao and C.-H. Zhou, *Eur. J. Med. Chem.*, 2024, 275, 116626.
- 32 X. Yu, X. Cai, S. Li, L. Luo, J. Wang, M. Wang and L. Zeng, *Food Chem.*, 2022, **366**, 130422.
- 33 D. Chahar, B. Yadav and P. Venkatesu, ACS Appl. Nano Mater., 2024, 7, 26202–26214.
- 34 D. M. Byler and H. Susi, Biopolymers, 1986, 25, 469-487.
- 35 H.-Y. Sui, D. Chen, J.-P. Huang, Z.-Y. Hu, L. Hu, J.-H. Shi and S.-L. Jiang, Spectrochim. Acta, Part A, 2025, 326, 125197.
- 36 K. Du, X. Du, Z. Sun, Y. Wang, Y. Bao, J. Lan, R. Shi and Z. Zhao, *Colloids Surf.*, A, 2024, 685, 133218.
- 37 S. Cometta, B. C. Donose, A. Juárez-Saldivar, A. Ravichandran, Y. Xu, N. Bock, T. R. Dargaville, A. D. Rakić and D. W. Hutmacher, *Bioact. Mater.*, 2024, 42, 68–84.